Measuring currents, ice drift, and waves from space: the Sea Surface KInematics Multiscale monitoring (SKIM) concept

Fabrice Ardhuin[1], Yevgueny Aksenov[2], Alvise Benetazzo[3], Laurent Bertino[4], Peter Brandt[5],
Eric Caubet[6], Bertrand Chapron[1], Fabrice Collard[7], Sophie Cravatte[8], Frederic Dias[9],
Gerald Dibarboure[10], Lucile Gaultier[7], Johnny Johannessen[4], Anton Korosov[4], Georgy Manucharyan[11],
Dimitris Menemenlis[12], Melisa Menendez[13], Goulven Monnier[14], Alexis Mouche[1], Frederic Nouguier[1],
George Nurser[2], Pierre Rampal[4], Ad Reniers[15], Ernesto Rodriguez[12], Justin Stopa[1], Celine Tison[10],
Marion Tissier[15], Clement Ubelmann[16], Erik van Sebille[17], Jérôme Vialard[18], and Jiping Xie[4]

[1]Laboratoire d'Océanographie Physique et Spatiale (LOPS), Univ. Brest, CNRS, Ifremer, IRD, Brest, France
[2]National Oceaongraphic Center, Southampton SO14 3ZH, UK
[3]Institute of Marine Sciences, National Research Council (ISMAR-CNR), Venice, Italy
[4]Nansen Environmental and Remote Sensing Center, Bergen, Norway
[5]GEOMAR Helmholtz Centre for Ocean Research Kiel, Kiel, Germany
[6]Thales Alenia Space, Toulouse, France
[7]OceanDataLab, Locmaria Plouzané, France
[8] LEGOS, Université de Toulouse, CNES, CNRS, IRD, Toulouse, France
[9]University College, Dublin, Ireland
[10]CNES, Toulouse, France
[11]Division of Geological and Planetary Sciences, California Institute of Technology, Pasadena
[12]Earth Sciences Division, Jet Propulsion Laboratory, California Institute of Technology, Pasadena, California
[13]Environmental Hydraulics Institute "IH Cantabria" Universidad de Cantabria, Santander, Spain
[14]SCALIAN ALYOTECH, Rennes, France
[15]Department of Hydraulic Engineering, Delft University of Technology, Delft, Netherlands
[16]CLS, Toulouse, France
[17]Utrecht University, The Netherlands
[18]Sorbonne Universités (UPMC, Univ Paris 06)-CNRS-IRD-MNHN, LOCEAN Laboratory, IPSL, Paris, France

Correspondence to: Fabrice Ardhuin (ardhuin@ifremer.fr)

Abstract. We propose a new satellite mission that uses a near-nadir Ka-band Doppler radar to measure surface currents, ice drift and ocean waves at spatial scales of 40 km and more, with snapshots at least every day for latitudes 75 to 82, and every few days otherwise. The use of incidence angles at 6 and 12 degrees allows a measurement of the directional wave spectrum which yields accurate corrections of the wave-induced bias in the current measurements. The instrument principle, algorithm for current velocity and mission performance are presented here. The proposed instrument can reveal features on tropical ocean and marginal ice zone dynamics that are inaccessible to other measurement systems, as well as a global monitoring of the ocean mesoscale that surpasses the capability of today's nadir altimeters. Measuring ocean wave properties facilitates many applications, from wave-current interactions and air-sea fluxes to the transport and convergence of marine plastic debris and assessment of marine and coastal hazards.

1 Introduction

Because the ocean surface is the interface between ocean, atmosphere and land, surface currents play an important role in defining the fluxes of heat, momentum, carbon, water, etc. between Earth System components. The ocean surface velocity

5   combines surface currents (mainly driven by winds, density gradients, and tides), with a wave-induced drift, known as Stokes drift. This total mass movement transports surface heat, salt and everything that is in the upper ocean, natural or man-made, including marine plastic debris (van Sebille et al., 2015). While vastly improving over the satellite era, there are still important gaps in our knowledge of ocean currents and waves. Satellite altimeters have been around for over 20 years, but along-track sea level anomaly and significant wave height are not sufficient to characterize the multi-scale motions of the oceans. This is

10   particularly true near the equator (Cravatte et al., 2016), around the edge of the sea ice (Korosov and Rampal, 2017), and in strong western boundary currents (Rouault et al., 2010; Rio et al., 2014). Other available measuring systems are very local, such as HF radars, or global with a sparse coverage, such as drifters (e.g. Elipot et al., 2016). As shown on figure 1, a single polar orbiting satellite with a swath width of 270 km could extend the capability of existing systems for monitoring ocean surface velocities, in particular for wavelengths between 60 and 1000 km and periods ranging from 3 days to 30 days.

15   Measurements of ocean surface velocities from remote sensing platforms have used a wide range of techniques. The most widely used at large scales include satellite altimeters, possibly combined with scatterometer wind and in situ drifters (e.g. Bonjean and Lagerloef, 2002; Sudre et al., 2013; Rio et al., 2014). Other techniques such as image processing of optical or Synthetic Aperture Radar (SAR) imagery have been demonstrated in many regions (see Isern-Fontanet et al., 2017, for a review). Direct measurements of ocean surface velocity using Doppler techniques are now widely used in land-based radar

20   systems, with operational use for current mapping in the high-frequency band, ranging from 3 to 30 MHz (Barrick, 1972). Interesting results have also been reported with land-based microwave radars (Forget et al., 2006, 2016), but the measured velocity is not fully understood.

Airborne and space-based measurements of surface velocity have been performed with across-track interferometric (ATI) SARs using two antennas (Goldstein and Zebker, 1987). This has been generalized to squinted ATI SARs to provide the two

25   components of the current vector (Buck, 2005; Wollstadt et al., 2016). More recently, Chapron et al. (2005) have shown the potential of using the Doppler centroid of ocean backscatter received by a single antenna. Although this measurement is more noisy than ATI, resulting in an effective coarser resolution, the velocity given by the Doppler centroid is equivalent to an ATI measurement (Romeiser et al., 2013). Hence, the Doppler centroid method is a cost-effective solution for deriving current information from existing satellite missions such as Envisat and the Sentinel 1 constellation. This has already led to scientific

30   application on the monitoring of intense currents (Rouault et al., 2010).

This demonstration of Doppler oceanography from space, using measurements of opportunity, has led us to propose a specially built Doppler radar altimeter that uses nadir and off-nadir beams in Ka-band. This is the Sea Surface KInematics Multiscale monitoring (SKIM) mission. SKIM is designed to measure both the horizontal surface velocity vector (U, V), i.e.
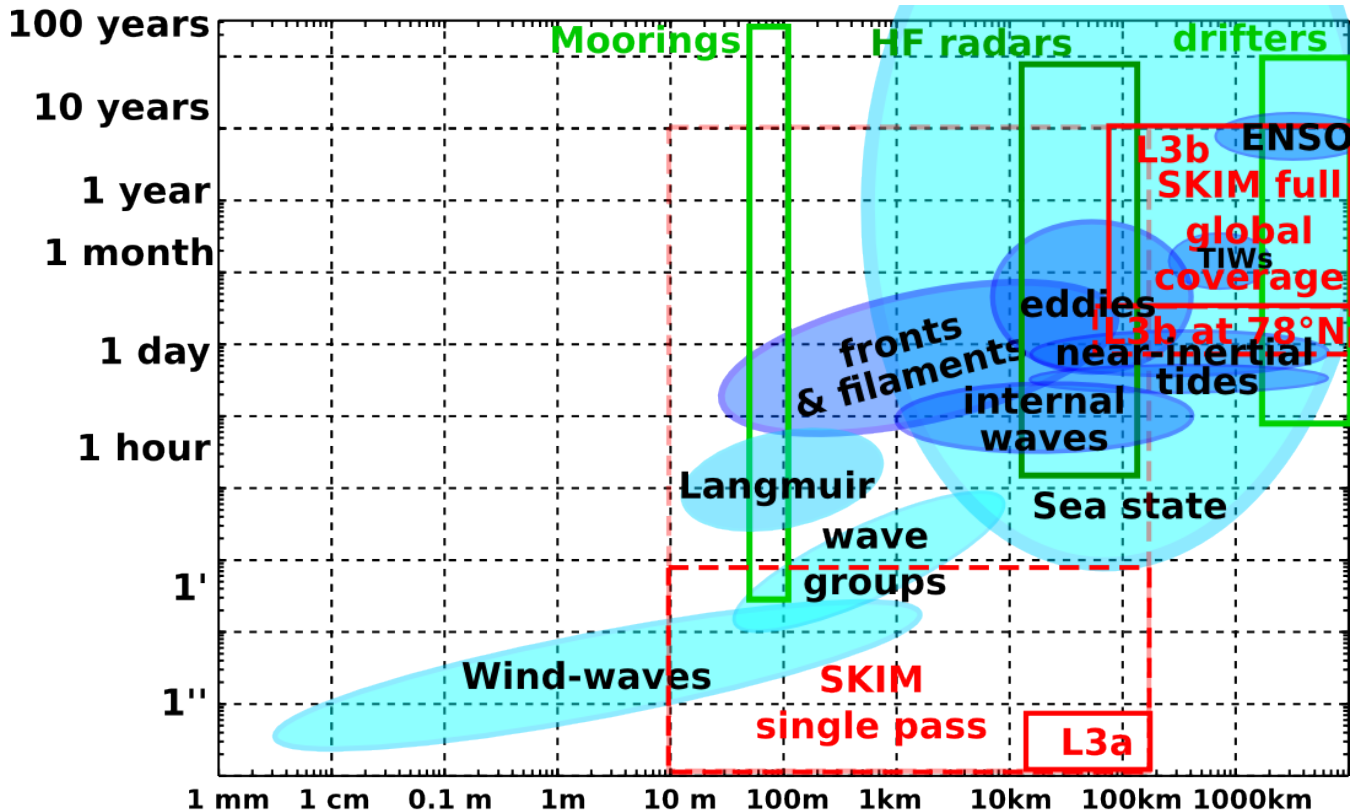
Figure 1. Typical periods and wavelengths of processes that contribute to the surface velocity. Ocean circulation processes are in dark blue, wave-related processes are in light blue. Scales resolved by existing measuring systems appear in green, and our proposition of a Sea surface KInematics Multiscale (SKIM) satellite mission in red, with different scales resolved in a single pass level 3a product (L3a), or the full time history of the measurements gridded as a level 3b product (L3b). Note that a limited coverage in space or time leads to aliasing of the unresolved scales (e.g. Stammer et al., 2000; Gille and Hughes, 2001).

surface current or ice drift, and the directional wave spectrum $E(k,\theta)$ where k is the wavenumber and θ is the azimuth of wave propagation. Wave spectra are used to correct for a wave-induced bias in the Doppler velocity. The purpose of the present paper is to describe the measurement principle and the expected instrument performance.

Doppler measurements start from a line of sight velocity U_{LOS} which contains a very large non-geophysical component
5   U_{NG} due to the relative motion of the spacecraft relative to the solid Earth. The anomaly relative to U_{NG} can be interpreted as a horizontal geophysical Doppler contribution,

$$U_{\mathrm{GD}} = (U_{\mathrm{LOS}} - U_{\mathrm{NG}})/\sin(\theta_i) \qquad (1)$$

where θ_i is the local incidence angle. The geometry of the measurement is illustrated in Figure 2.

Common to ATI and Doppler centroid techniques, is the contribution of orbital velocity of wind-waves to the geophysical
10   velocity U_{GD}, in the form of a wave bias U_{WB} (Chapron et al., 2005; Mouche et al., 2008; Martin et al., 2016). As a result, the
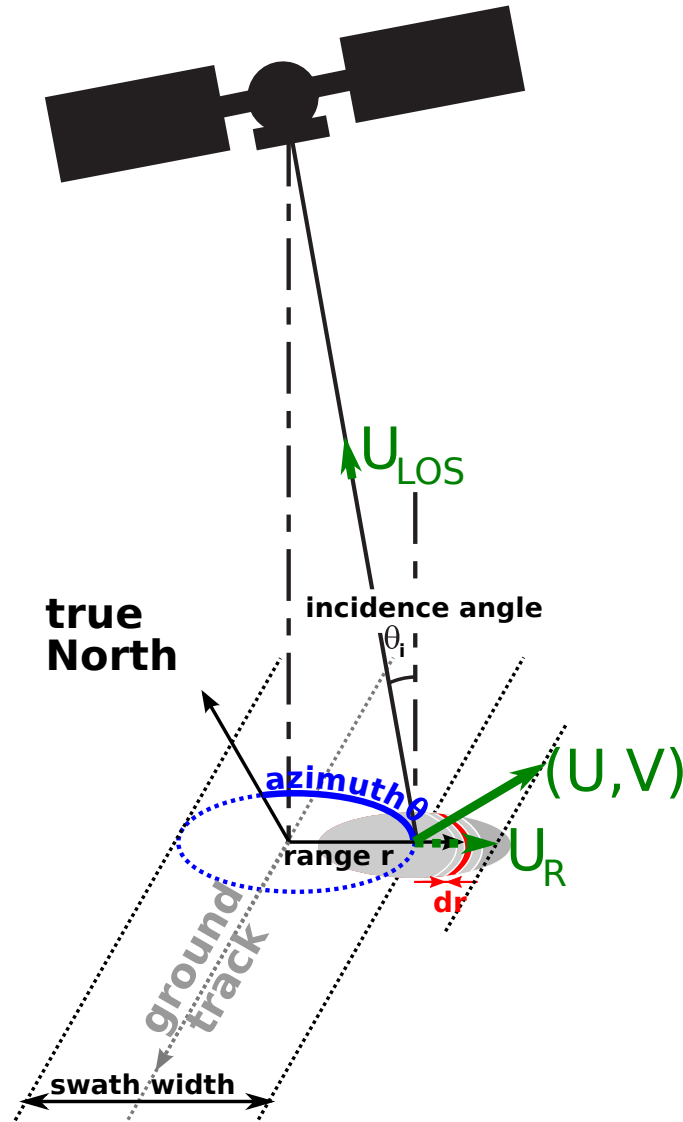
Figure 2. Geometry of measurement from a radar with a local incidence angle θ_i, looking towards azimuth θ. For simplicity of the schematic, we have taken $U_{\mathrm{WB}} = 0$ and $U_{\mathrm{NG}} = 0$, so that the line of sight velocity is simply $U_{\mathrm{LOS}} = (U \sin\theta + V \cos\theta) \sin\theta_i$. Note that the diameter of the footprint (6 km) is exaggerated compared to the swath width (270 km) for readability.

radial current, projected on the mean sea surface in the azimuth of radar look, is given by

$$U_R = (U_{\mathrm{GD}} - U_{\mathrm{WB}}). \qquad (2)$$

U_R is the radial component of the Lagrangian mean velocity vector (U, V), defined from the average drift velocity of water parcels. This Lagrangian mean drift is $\mathbf{U} = \mathbf{U}_E + \mathbf{U}_S$, the vector sum of a quasi-Eulerian current (Jenkins, 1989) $\mathbf{U}_E$ and a

Stokes drift $\mathbf{U}_S$ (Stokes, 1849). $\mathbf{U}_S$ is the drift motion due to waves that arises from a correlation between the displacement and velocity field. Its magnitude at the sea surface U_S is of the order of 1.0 to 1.8% of the wind speed, typically larger than the local wind-induced quasi-Eulerian current known as the Ekman current, unless a strong stratification is present (Ardhuin et al., 2009).

5   Previous applications have used the radial wind speed $U_{10,R}$ projected in the range direction as a proxy for estimating U_{WB}. As we review in section 2, this wind speed proxy is not sufficient for obtaining accurate instantaneous current velocities. We therefore propose in section 3 an algorithm for estimating U_{WB} within 10 to 20%, based on the measurement of the directional wave spectrum also performed by SKIM. This joint measurement of currents and waves is the basis of the SKIM measurement concept. Its expected overall performance and effective resolution is described in section 4. A summary and perspectives on
10   applications and improvement in the processing follow in section 5.

2   Importance of mean slope speed or Stokes drift

2.1   Expected and observed dependence of U_{WB}

Because the velocity or phase shift recorded by a radar corresponds to the velocity weighted by the back-scattered power, the wave-induced bias U_{WB} is related to the mean slope velocity vector, $\mathbf{msv} = (<\partial^2\zeta/\partial x\partial t>, <\partial^2\zeta/\partial y\partial t>)$, due to the
15   correlation between the normalized radar cross section (NRCS or σ_0) and the surface slope (e.g. Nouguier et al., 2016). For linear waves, $\mathbf{msv}$ is equal to twice the surface Stokes drift vector (U_S, V_S).

In practice U_{WB} is very close to a gain factor G multiplied by the surface Stokes drift projected on the range direction $U_{S,R}$ as described by Chapron et al. (2005). G is a function of radar frequency, incidence angle, and sea state. Figure 3 shows the expected dependence of G on the incidence angle for average wind speeds and a fully developed sea state, using a physical
20   optics model or its Kirchoff approximation (The SKIM Team, 2017). A typical order of magnitude in Ka-band for incidence angles less than 15 degrees, is $G \simeq 25$, which is similar to values in C-band at higher incidence angles.

This dependency of U_{WB} on the radial Stokes drift $U_{S,R}$ and incidence angle θ_i, as well as the order of magnitude of G are confirmed by the analysis of platform-based measurements by Yurovsky et al. (2017), and airborne measurements from the AirSWOT instrument (The SKIM Team, 2017).

2.2   Estimation of U_{WB}

The surface Stokes drift vector (U_S, V_S) can be estimated from the wave spectrum, assuming linear wave theory (Kenyon, 1969). For waves in deep water this is

$$(U_S, V_S) = 2\sqrt{g}\int\limits_0^{2\pi}\int\limits_0^{\infty}(\sin\theta, \cos\theta)k^{1.5}E(k,\theta)\mathrm{d}k\mathrm{d}\theta, \tag{3}$$

which can be measured from the first moments of directional wave buoys (Kuik et al., 1988). In the absence of directional
30   measurements, only a non-direction Stokes drift is available $U_{S,\mathrm{nd}} = 2\sqrt{g}\int_0^{\infty}k^{1.5}E(k)\mathrm{d}k$, which is about 50% larger.
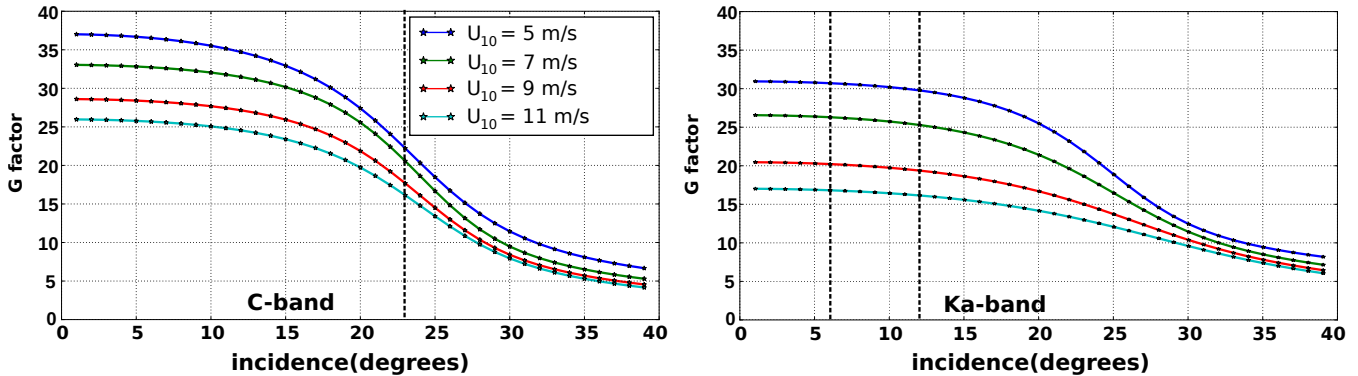
Figure 3. G factor estimated using a Kirchoff approximation, for a wave spectrum given by Elfouhaily et al. (1997), representing a fully developed sea state for wind speeds U_{10} ranging from 5 to 11 m/s. left: C band, appropriate for Envisat and Sentinel 1, right: Ka band for SKIM.

The projected Stokes drift $U_{S,R}$ is correlated with the wind speed in the radial direction $U_{10,R}$. Hence, the approximation of U_{WB} as a function of $U_{10,R}$ is a logical first step proposed by Chapron et al. (2005) and Mouche et al. (2008), and used by Rouault et al. (2010) to retrieve surface currents.

However, for a given wind speed the sea state introduces a typical variation of $U_{S,R}$ that has a standard deviation of 40%.

5   Further, the distribution of $U_{S,R}$ as a function of $U_{10,R}$ can change significantly from one region of the ocean to another. These properties are illustrated in figure 4 with data for the years 2011 to 2015, from the North-East Pacific station PAPA, in deep water (Thomson et al., 2013), and a North-East Atlantic coastal buoy Pierre Noires, in 60 m depth (Ardhuin et al., 2009). In both cases the wind speed is taken from operational ECMWF analyses. Directional wave moments were downloaded from CDIP and CEREMA. The Stokes drift was integrated over the frequency range of the Datawell Waverider buoy, from 0.025 to

10   0.58 Hz.

Using the order of magnitude $U_S \approx 0.01 U_{10}$, the sea-state variation means that a wind-only proxy for U_{WB} gives a root mean square (rms) error on the current that of the order of $40\% \times G \times 0.01 = 10\%$ of the wind vector. With a median wind speed of 7 m/s, this is a 70 cm/s error in the wind direction for C-band at $23°$ of incidence, or Ka-band at $12°$. Such a high value is not acceptable for a single satellite pass, but these errors cancel out when the Doppler velocity is averaged over many

15   satellite passes, 10 or more, as done by Collard et al. (2008) and Rouault et al. (2010).

Even at the higher incidence angles of $58°$ proposed by Bourassa et al. (2016), for which we expect $G \simeq 7$ in Ka-band, the wave bias is reduced by a factor 4, but the rms error on U_{WB} is still significant at 20 cm/s, even if there is no error on the wind. Larger incidence angles also suffer from lower backscatter levels and thus a larger instrumental error in the raw line of sight velocity U_{LOS}.

20   A possible intermediate approach is to use a numerical wave model to estimate $U_{S,R}$, with typical errors ranging from 15 to 20% in open ocean and deep water conditions according to Rascle and Ardhuin (2013). Yet, recent investigations by Ardhuin
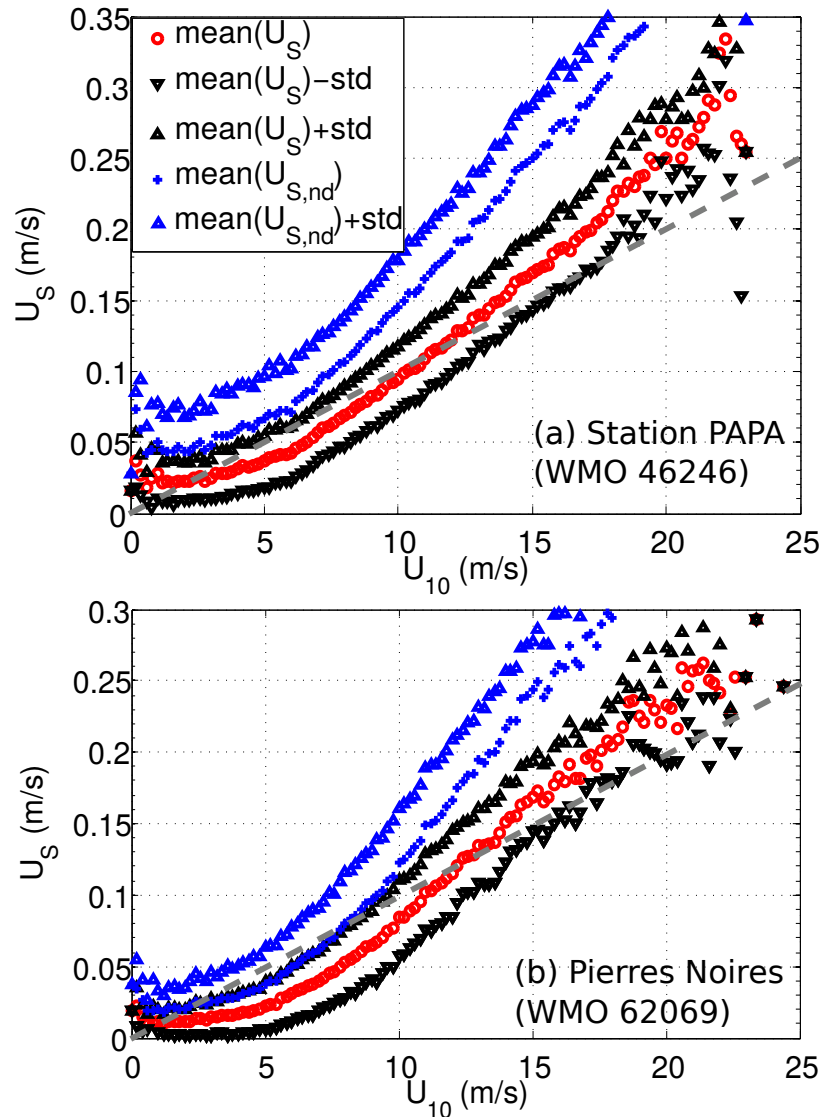
Figure 4. Example of mean value (in red) of the Stokes drift vector norm $U_S = |(U_S, V_S)|$ as a function of wind speed for two locations: station PAPA in the North-East Pacific, and buoy 62069 off the French Atlantic coast. The black symbols show the mean plus or minus one standard deviation for each wind speed. The dashed grey line is $U_S = 0.01 U_{10}$. For both buoys, the non-directional Stokes drift (in blue) is about 50% higher.

et al. (2017b) on the impact of ocean currents on small scale sea state variations suggest that it may be difficult to separate the gradients in wave bias from the surface current at scales under 100 km.

Another more radical approach is to measure the sea state properties necessary for the evaluation of $U_{S,R}$, in addition to the Doppler velocity U_{LOS}. In general $U_{S,R}$ can be estimated from the directional wave spectrum. The details of this estimation

with a rotating wave Doppler spectrometer, combining the ideas of Jackson et al. (1985) and Caudal et al. (2014), is presented in Appendix A. An overall accuracy of 10% for $U_{S,R}$ is expected from our preliminary algorithm.

3 Restitution of the total surface velocity

The algorithm proposed to retrieve the field of surface velocity vectors and wave spectra is summarized in Figure 5.

Instrument data
P(r) for each cycle

Instrument data
U_{LOS}(r) for each cycle

Auxiliary data

Level 1 waves
1D spectra of σ_0 and U

Level 1 mean velocity
U_{NG} (r)   & U_{GD} (r)

Level 2 waves
E(k,θ) spectrum
$U_{S,R}$ & gain factor G

Level 2 mean velocity
$U_{WB} = G \times U_{S,R}$
$U_R = U_{GD} - U_{WB}$

Level 3b mean velocity
multiple-swath maps
$\mathbf{U}_E = (U_E , V_E) = \mathbf{U}_S - \mathbf{U}$

Level 3a mean velocity
single-swath maps
$\mathbf{U} = (U,V)$ & $\mathbf{U}_S = (U_S, V_S)$
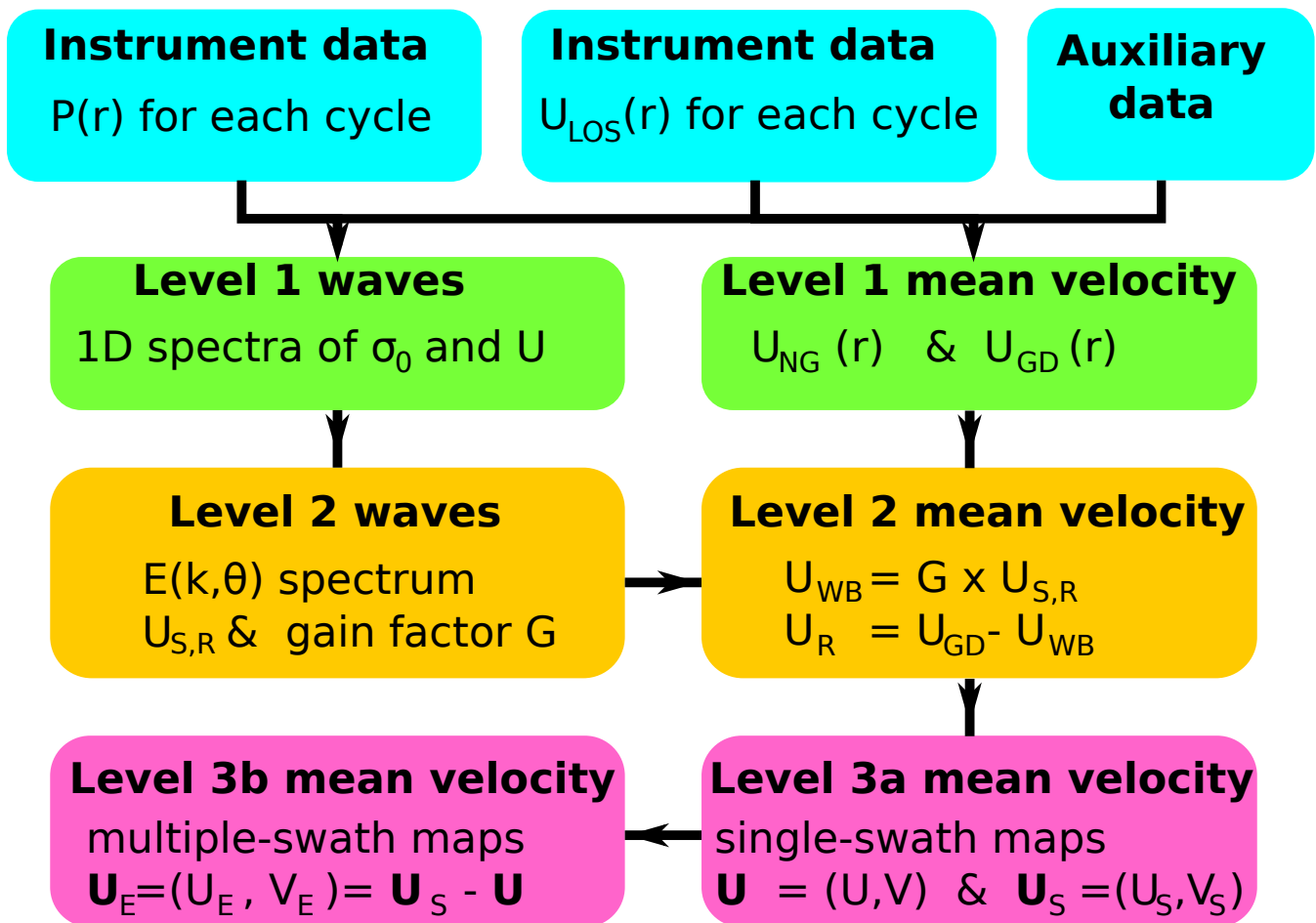
Figure 5. Logical tree going from Level 0 raw data to Level 3 gridded fields of surface velocity and wave parameters. For gridding with multiple satellite passes, we propose to use the quasi-Eulerian surface velocity defined as $\mathbf{U}_E = \mathbf{U} - \mathbf{U}_S$ (Jenkins, 1989).

5   The elementary measured quantities are the power P and velocity U_{LOS} as a function of the range r within each footprint of diameter 6 km, with a resolution dr that is less than 4 m for $\theta_i = 12°$. Hence, these basic measurement are highly resolved in range but averaged over the footprint diameter in the perpendicular (azimuthal) direction. This averaging is the basic principle

of the wave spectrometer laid out by Jackson et al. (1985). Namely, only the waves aligned with the line of sight produce a modulation of the signal in the range direction.

Several effects introduce measurement errors. We have particularly investigated the following three terms in the error budget for the level 2 data (radial current velocity U_R),

5   – $\mathrm{err_{DC}}$: The Doppler centroid estimation error is a function of the strength of the radar backscatter, hence of the incidence angle, radar transmitted power, altitude and averaging. Using broad margins (e.g. using only half of the rated Ka-band power) this was estimated to be under 10 cm/s at $\theta_i = 12°$ and in the absence of ice (The SKIM Team, 2017). This error is a well known function of the azimuth relative to the satellite ground track.

     – $\mathrm{err_{PA}}$: The platform attitude error was found to be negligible in all cases thanks the rotating beam. This is because any
10   small mispointing that varies slowly in time produces a clearly identifiable pattern as a function of azimuth. This is detailed in Appendix B.

     – $\mathrm{err_{WB}}$: The wave bias error is explained and justified in Appendix A. We have performed a detailed analysis on the error $\mathrm{err}(U_{S,R})$ in the estimation of the radial Stokes drift $U_{S,R}$ over each footprint, which contributes to $\mathrm{err_{WB}}$ amplified by the G factor. Errors in the estimation of the G factor are not so easy to model but, for a given mean square slope, G
15   is expected to have a weak dependence on sea state properties and also G can be given directly from the ratio of the Doppler and σ_0 spectra. We have therefore assumed that errors on the estimation of G should not cause an error larger than the error due to uncertainties in $U_{S,R}$. Hence we used $\mathrm{err_{WB}} = 2G\,\mathrm{err}(U_{S,R})$

We have not considered the particular cases of extremely low backscatter, for wind speeds under 2 m/s, in which the three errors can be correlated, and we have assumed that these 3 error sources are uncorrelated.

20 ## 4   Overall performance and effective resolution

4.1   From radial components to gridded vector fields

Here we show results corresponding to one particular set-up of the SKIM radar, which is called 'SKIM2' in The SKIM Team (2017). This configuration uses 8 beams, with one beam at nadir ($\theta_i = 0$), two beams at 6° and 5 beams at 12°. These beams rotate at 3.14 rotations per minute (one turn in 17.5 s) thanks to the rotation of a plate carrying feed horns arranged as shown
25 in Figure 6.a. The horns are placed at the focal point of a parabolic reflector, similar to the wave scatterometer SWIM (Hauser et al., 2017) which is carried by the China-France Ocean Satellite (CFOSAT) mission. The main differences between SWIM and SKIM are the radar frequency (Ka instead of Ku band, giving smaller footprints), and the Doppler capability of SKIM.

Using incidence angles up to 12° and altitude of 695 km gives swath width of 270 km as shown in Fig. 6.b. For each beam, we have 60 measurement cycles of 1024 pulses for each complete turn, each cycle is 36.6 ms long. The radar pulse
30 repetition frequency is 32 kHz. The line-of-sight velocity is determined from the phase shift between consecutive pulses. These parameters define the instrument error $\mathrm{err_{DC}}$, as listed in table 1.
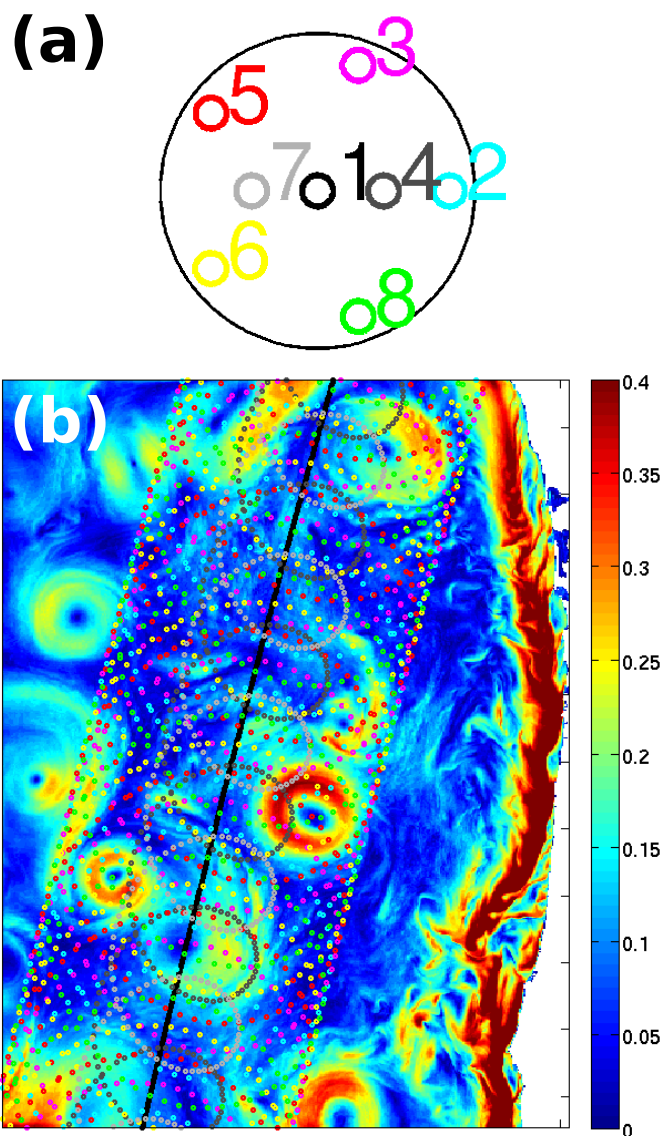
Figure 6. (a) Pattern of beams (1 is nadir, 4 and 7 are at 6°, the others at 12° incidence). The different colors help associating the footprint patterns in (b) with each beam. Background colors in (b) represent simulated currents velocities off the Oregon coast (in m/s), courtesy of Y. Chao, previously used by Fu and Ubelmann (2014) for the evaluation of the SWOT mission performance.

The other important source of error, caused by inaccuracies in the wave bias correction is a function of the beam geometry but also of the strength of gradients of the Stokes drift, which are mostly caused by current gradients (Ardhuin et al., 2017b). This wave bias error is estimated following the method laid out in Appendix A.

Finally, the last important source of error we have investigated is the mapping error, going from Level 2 data at each footprint 5   to Level 3 data on a regular grid. This mapping error is similar to what happens with HF radars (e.g. Lipa and Barrick, 1983;

Table 1. Summary of expected root mean square errors for Level 2 radial velocity (for $\theta_i = 12°$) and along-track Level 3a (single swath snapshot) or zonal Level 3b (multi-swath time-evolving field) velocity component, based on the preliminary algorithms in the case of the SKIM2 configuration (open burst, 8 beams).

Region	Equator	Fram (open water)	Fram (ice)	Gulf Stream	Oregon coast
err_{DC}	< 0.1 m/s	< 0.1 m/s	< 0.1 m/s	< 0.01 m/s	< 0.01 m/s
err_{PA}	< 0.01 m/s	< 0.01 m/s	< 0.01 m/s	< 0.01 m/s	< 0.01 m/s
err_{WB}	0.05 m/s	0.08 m/s	0.02 m/s	0.15 m/s	0.13 m/s
L3a, L_e	89 km	59 km	TBD	65 km	90 km
L3a error	0.03 m/s	0.11 m/s	TBD	< 0.09 m/s	0.04 m/s
L3b, L_e	290 km	62 km	TBD	71 km	95 km
L3b error	0.14 m/s	0.12 m/s	TBD	0.23 m/s	0.09 m/s

Kim et al., 2008). In particular, SKIM only measures radial components so that on the edges of the swath only the cross-track component is measured, and in the center there are only measurements of the along-track component, as shown in figure 7.

The use of the two incidence angles, 6 and 12°, allows to fill the swath and obtain cross-track measurements closer to the center of the swath. We can also use the nadir altimeter beam to obtain cross-track geostrophic velocities. An optimal
5 interpolation method specially designed to including covariances between the two current components has been adapted to also include this additional nadir data (The SKIM Team, 2017).

The combination of these three errors gives the total error that must be compared to the magnitude of the current. We have therefore defined an effective resolution wavelength L_e as the scale above which the total error is larger than the signal, as shown in Figure 8 for the case of the Gulf Stream.
10 The overall error depends on many factors related to the patterns in ocean currents and the instrument parameters. We have estimated all errors in particular ocean conditions, using state of the art models for the ocean circulation (e.g. Rocha et al., 2016; Gula et al., 2015) and associated ocean waves (Ardhuin et al., 2017b). Model simulations were performed at resolutions on the order of 1.5 km for a set of regions for which we expect SKIM to have a strong contribution, resolving processes that are not accessible with today's observing systems. These include an Arctic region with strong currents (Fram Strait), an equatorial
15 region (in the Atlantic around 23°W), a western boundary current (the Gulf Stream) and a coastal region (Oregon).

The root mean square error on current components and the resulting effective resolution are summarized in Table 1, but they are better understood by comparing maps of currents from the simulated SKIM processing to the input modeled currents. Several examples are given by The SKIM Team (2017). It is also interesting to compare the results of different observing systems.
20 An important outcome of the SKIM simulations is that a wide swath is necessary to obtain the shorter revisit time needed to monitor the smaller ocean structures that evolve more rapidly. Interferometric SAR technology will be used to produce a 120 km wide swath for the Surface Water Ocean Topography (SWOT) mission (see Figure 9).
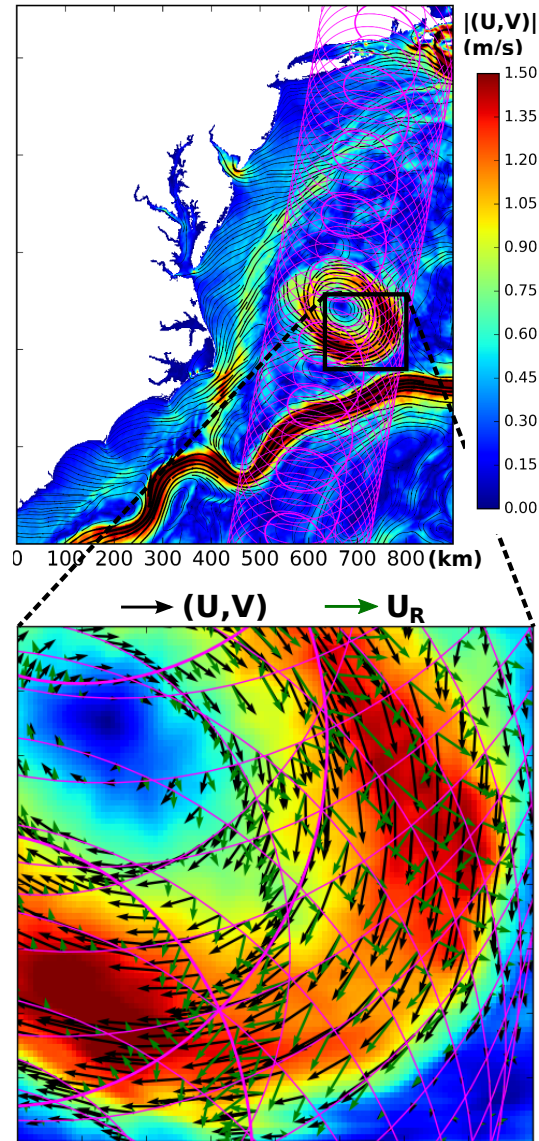
Figure 7. Illustration of current components U and V and radial component U_R in the case of the Gulf Stream.

The narrower swath gives a larger revisit time at mid-latitudes of 10 days with SWOT instead of 4 days with SKIM. As a result, only larger scale motions can be monitored with SWOT, with an effective wavelength $L_e = 115$ km in the Gulf Stream region, instead of 71 km with SKIM. The Doppler scatterometer mission proposed by Bourassa et al. (2016) has a much wider swath, about 1800 km, and is designed to measure wind and current vectors. Because it measures at larger incidence angles for which signals are weaker, an accurate current estimate requires averaging over several passes, thereby reducing the effective
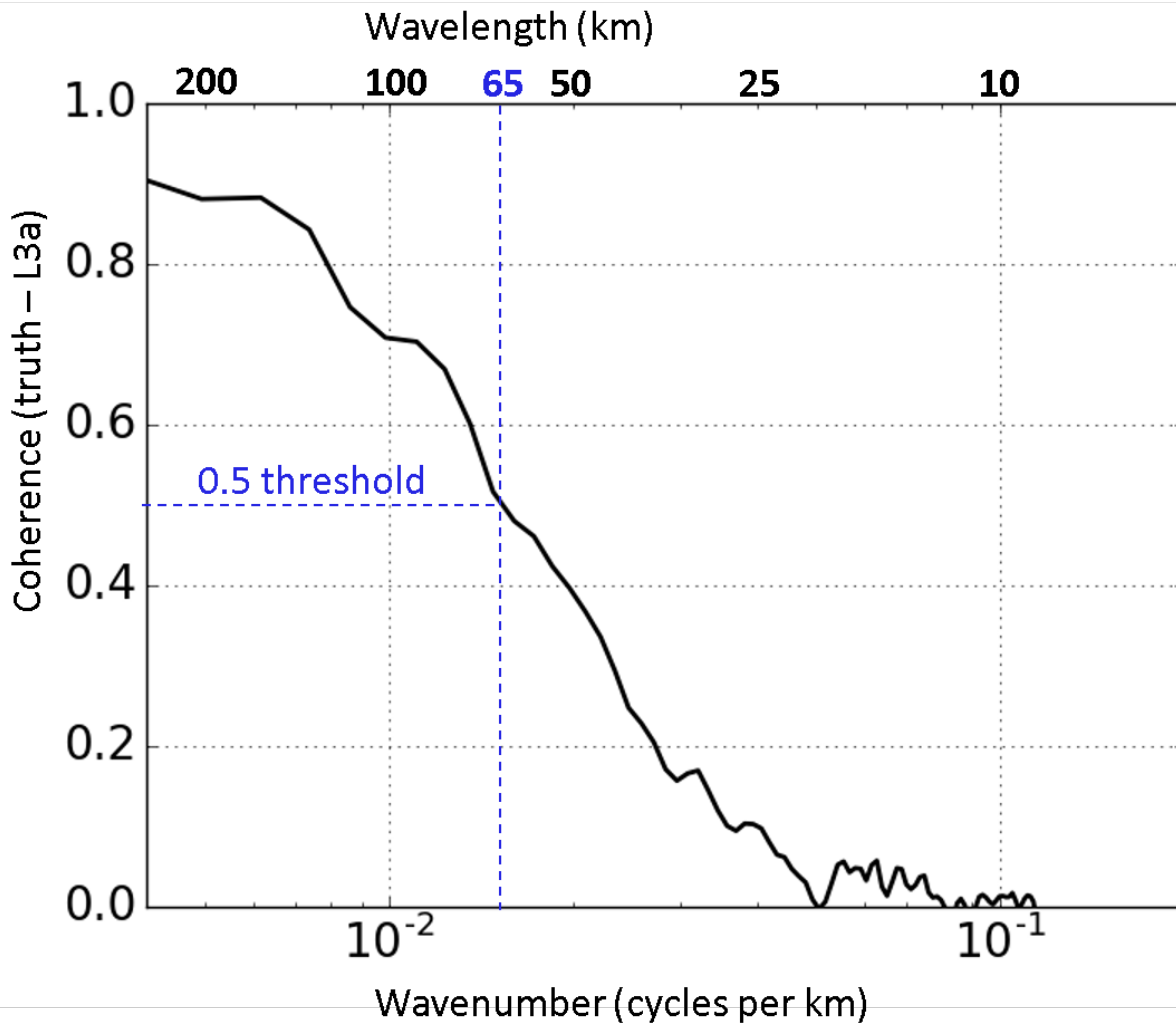
Figure 8. Average coherence of simulated SKIM Level 3a current with the "truth" provided by MITgcm simulations, in the case of the Gulf Stream, for October 2011.

temporal resolution. As a result, this is a great instrument for vector wind measurements but it is not clear if it would perform better than SKIM for current measurements.

In the case of SWOT, the interpretation of the sea surface height (SSH) in terms of current relies on the geostrophic equilibrium. Unbalanced motions, such as internal waves, also contribute to the SSH. As a result, the usual simple interpretation of the SSH in terms of currents contains small scale noise associated to ageostrophic motions, shown in Figure 9.c,d. The separation of balanced and unbalanced motions is the topic of active research (e.g. Ponte et al., 2017).
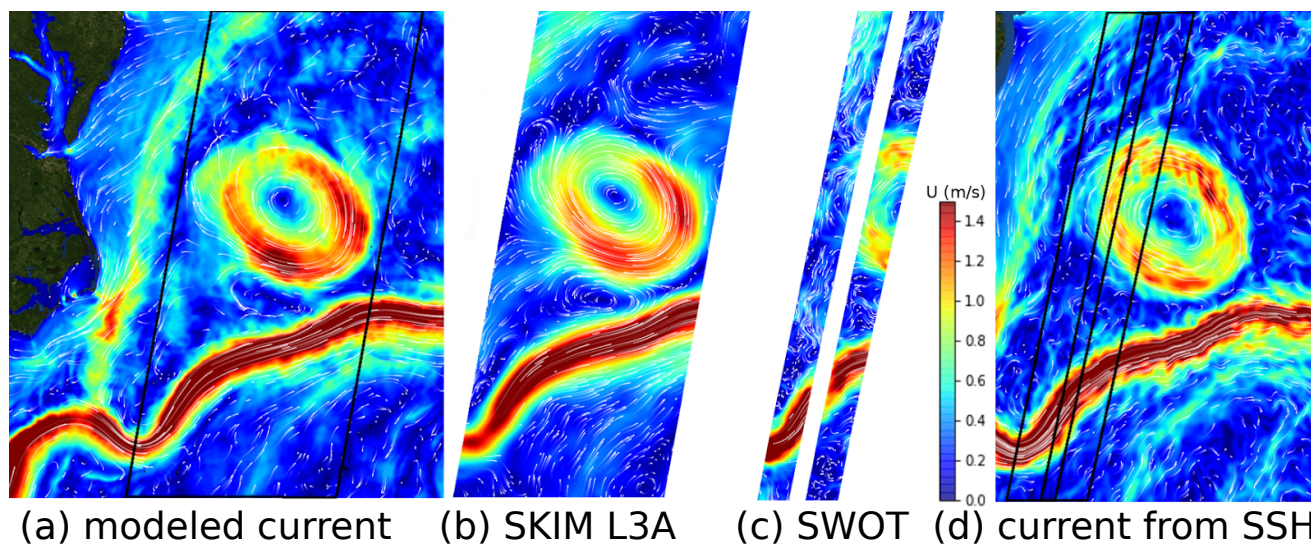
Figure 9. Simulated ocean currents over the Gulf Stream, and associated SKIM and SWOT simulated observations for a single satellite pass.

dynamical methods of interpolation (Ubelmann et al., 2016), not considered here, can probably further improve on the restitution of temporal evolutions, and thus the reduction for L_e for L3b products from both SWOT and SKIM.

4.2 Challenges and opportunities over sea ice

The Marginal Ice Zone (MIZ) in the Arctic is expanding (e.g. Aksenov et al., 2017). This important region of the world
5 ocean will not be well monitored in terms of currents by existing and planned satellite missions. Ice concentration is the only parameter that is well monitored near the ice edge, with difficulties in recovering ice thickness and ice drift (Korosov and Rampal, 2017). The very rich dynamics across the ice edge offer great opportunities for Doppler-based measurements. In particular, narrow ice jets and eddies are observed in satellite imagery (Johannessen et al., 1983) and reproduced in high resolution models (Horvat et al., 2016).
10 These features cannot be monitored by today's altimetry due to their small scale and the changes in waveform shapes from open water to ice. In the ice, the wave-induced bias becomes negligible as the wave amplitude is strongly attenuated. On the contrary, the instrument noise is expected to increase by about a factor 2.5 due to a generally weaker (8 dB) back-scatter over ice compared to open ocean at incidence angles under $12°$ (The SKIM Team, 2017). A detailed analysis of errors right at the ice edge requires to take into account the strong variation in backscatter in all terms of the error budget. This is beyond the
15 scope of the present paper.

Also, it should be possible to measure waves in ice, without the SAR processing used by Ardhuin et al. (2017a) but using the Doppler spectrum and the modulation of the radar backscatter due to range bunching. Indeed, it is not clear how strong the tilt modulation is over the ice, but range bunching is maximum for a swell steepness $ka = \tan\theta_i$, which is 0.1 for $\theta_i = 6°$. A

swell steepness of 0.025, as in the Marginal Ice Zone observations reported by Sutherland and Gascard (2016), still produces a 20% (0.9 dB) modulation of σ_0.

5   Preliminary study of surface current impact

In order to evaluate the contribution of a surface Doppler measurement in an ocean forecasting system, we have used the

5   TOPAZ assimilation system, implemented in the Copernicus Arctic Marine Forecasting Center. This system uses a regional configuration of the HYCOM ocean model over the North Atlantic and Arctic Oceans and assimilates different types of satellite and in situ observations with an Ensemble Kalman Filter, running 100 dynamical members.

Each ensemble member receives random perturbations of the ocean surface conditions, including non-divergent random winds with an amplitude of 2.5 m/s (see Xie et al., 2017, for more information about the reanalysis). We have used the

10   simulated uncertainties of SKIM Level 2 surface velocities, following their description above, to produce a measure of the impact of assimilating SKIM surface currents in conjunction to all other observations on a typical weekly cycle of the TOPAZ reanalysis in May 2015, in a period of stable reanalysis operations following 24 years of data assimilation.

We measure the information content of the assimilated data using the Degrees of Freedom for Signal (DFS) (Cardinali et al., 2004). This DFS has a maximum value of 100 in the case of the EnKF used in TOPAZ. Target DFS values range from 0 to 10,

15   above which there is a risk of "over-assimilation" (Sakov et al., 2012). The observation impact is calculated for each grid cell, using knowledge of the space and time location of the observations, their uncertainty estimates, but not the actual observed values. Since all observations are assimilated jointly, the impact of one observation type reduces that of the other types. The DFS values are dependent on the background and observation uncertainties specified in the TOPAZ system and are different in a different ocean data assimilation system.

20   Figure 10 exhibits the DFS values obtained by assimilating simulated SKIM surface currents together with other real measurements. The highest DFS appears in frontal regions like the Equatorial Counter-Current, the Gulf Stream and the Azores Current. The area near the Equator shows particularly high values as the impact of traditional altimeter data is limited by the vanishing of the Coriolis force. The South Atlantic is artificially removed as the simulated SKIM data used here only covers the North Atlantic.

25   The DFS indicate that SKIM provides the second largest impact overall, and the largest information content in the Gulf Stream and Equatorial regions for ocean data assimilation. It may seem counter-intuitive that the impact of surface currents from SKIM exceeds the impact of depth-averaged currents as of traditional altimeters in the Gulf Stream. This could be a transient effect due to the first-time assimilation of SKIM: the ensemble variance of surface currents may reduce on the following assimilation cycles and the DFS reduce accordingly. Alternatively it could be due to our assumption of negligible

30   representativity errors.

The results presented here only utilize the surface currents but not yet the surface waves nor the sea ice drift from SKIM. This observing system simulation experiment (OSSE) is highly simplified and does not resolve complex feedbacks of repeated
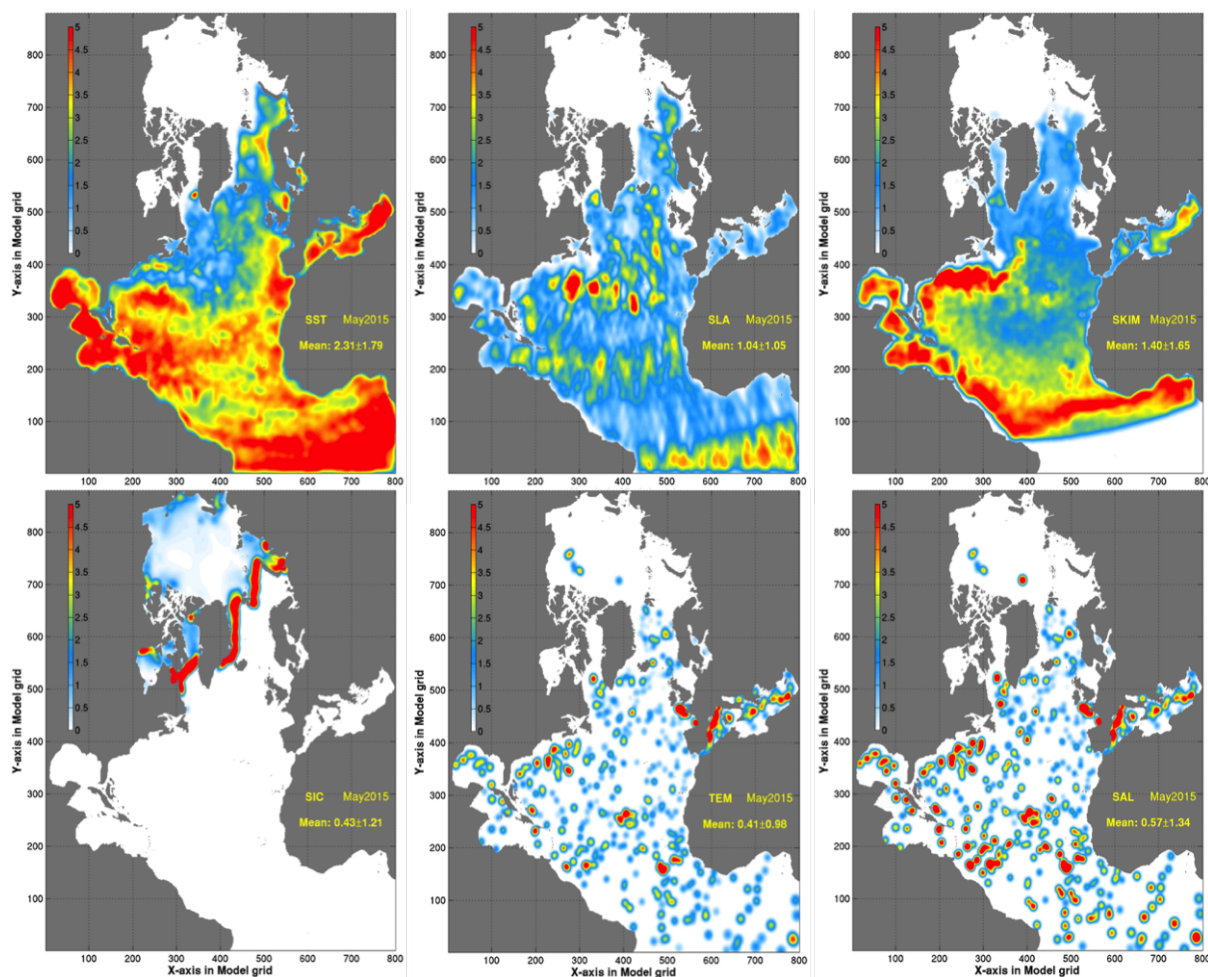
Figure 10. Degrees of Freedom for Signal of all assimilated observations during one week in May 2015. From Top line from left to right: OSTIA Sea Surface Temperature, CMEMS delayed-mode altimeter tracks, SKIM sea surface. Bottom line: OSI SAF Sea ice concentrations, in situ (incl. Argo) Temperature and Salinity profiles

data assimilation cycles. Still, this OSSE indicates that there is a scope for assimilation of sea surface currents in an operational forecasting system and that SKIM data should provide relevant information that is independent of existing ocean observations.

6 Conclusions and perspectives

Using nadir and near-nadir radar beams with Doppler measurements, the Sea surface KInematics Multiscale monitoring (SKIM) mission is designed to measure surface velocity vectors and ocean wave spectra. Measuring wave spectra down to wavelengths of 20 m, and possibly less, makes it possible to estimate the surface Stokes drift vector and correct for a strong wave-induced bias in the surface velocity vector, which is of the order of a gain coefficient G times the surface Stokes drift.

The use of a rotating beam pattern is critical in reducing errors caused by knowledge uncertainties in the platform attitude, which is today the main source of error in the level 2 surface current derived from the Sentinel 1 SAR constellation. We have chosen the same orbit as Sentinel-1C (S1C), except for a 4 degree shift to the East. This is a sun-synchronous orbit, with a 98.2° inclination, altitude 693 km and 12-day repeat cycle. The shift allows for a large overlap between SKIM and S1C on

5   ascending tracks that will be useful at least for calibration purposes.

The incidence angle of SKIM is limited to 12° by the choice of antenna technology that uses a rotating horn plate and fixed parabolic reflector. With this configuration, larger incidences lead to beam distortions. This geometry gives a swath width of 270 km and a relatively large signal to noise ratio thanks to the higher backscatter at these low incidence angles. Compared to the Envisat C-band measurements at incidence angles of 30° used by Rouault et al. (2010), in which case $G \simeq 10$, the error

10 on the wave bias is expected to be reduced by a factor 4 or more, allowing a single-pass estimation of the current components with an accuracy of the order of 0.1 m/s for a wavelength of about 60 km.

When the radial components are combined to produce maps of gridded vector velocity, the effective wavelength resolved, at which the signal is above the noise level, is of the order of 60 to 90 km for a single swath, depending on the pattern of currents. Except for latitudes 78 to 83° where the revisit time is less than one day, the effective resolution is degraded when the time

15 evolution of the currents is considered. At mid latitudes this gives $70 < L_e < 100$ km, due to the 3-day revisit time.

Further improvement on the accuracy and effective resolution may come from many improvements in radar settings (e.g. use of full power instead of 50%, and evolution in amplifier technology) which could give larger transmitted power and reduce the instrument noise $\mathrm{err_{DC}}$. Another source of improvement will be the reduction of wave bias error $\mathrm{err_{WB}}$, in which our estimation of errors on the G factor error may well be overestimated. Also, a combined analysis or assimilation of waves and

20 currents could properly take into account the correlations of waves and currents and lead to more accurate current estimates. Hence the error level and resolution found in our simulations are probably conservative.

Our results clearly shows that Doppler oceanography from space can be a very useful technique for monitoring space and time scales of the ocean circulation that are not well observed today. Future altimeter designs should probably consider adding off-nadir rotating beams for a more effective coverage of the ocean. In the present paper we have not discussed much the

25 added benefits of ocean wave measurements with unprecedented spectral and spatial coverage. These will be discussed in other publications. We only point out here that the sea state variability at small scales is probably dominated by the effect of ocean currents (Ardhuin et al., 2017b). It is thus logical to measure waves and currents together, and possibly further use the measured variability of sea state parameters to further constrain the magnitude of current gradients.

Code and data availability. Numerical model results presented in this article are available via ftp at the following address:

30 ftp://ftp.ifremer.fr/ifremer/ww3/HINDCAST/OTHER/SKIM/

Appendix A: Estimation of wave-induced bias U_{WB} from directional wave data

Wave spectra measurement from a rotating real aperture radar is discribed in detail in Jackson et al. (1985), and the additional use of Doppler measurements for removing the $180°$ ambiguity on the wave propagation direction was demonstrated by Caudal et al. (2014). As a result we will not discuss the accuracy of wave measurements, which is extensively discussed by Hauser et al. (2017) with a similar system, and only point out that SKIM should have more accurate wave spectra than SWIM due, among other factors, to a smaller footprint that leads to a larger amplitude of modulations, which scales as the the inverse of the footprint diameter. We will thus focus on the estimation of the wave-induced bias from the wave spectrum.

One important difficulty for the estimation of $U_{S,R}$ by projecting eq. (3) in direction θ, is that the Stokes drift contains contributions from all directions θ' whereas the measurement on a single footprint only give contributions in the look direction θ. For each footprint in azimuth θ' we only have the contribution of the waves propagating in direction θ', which we define as

$$
\begin{aligned}
U_{S,1D}(\theta') \;=\; & 2\sqrt{g}\int\limits_{0}^{k_{\max}} k^{1.5}E(k,\theta')\mathrm{d}k \\
& + F(k_{\max},\theta')E(k_{\max},\theta'),
\end{aligned} \tag{A1}
$$

where $k_{\max}$ is the wavenumber of the shortest resolved waves. Assuming that the spectrum of shorter waves rolls of like k^3 and neglecting non-linear effects gives $F(k_{\max},\theta') = \sqrt{g}k_{\max}^{2.5}$. For $k_{\max}$ corresponding to a 20 m wavelength (as expected for SKIM), hourly averaged measured spectra at station PAPA gives a typical random error of 6%. Waves shorter than 20 m are genrally less important due to a general broadening of the directional spectrum towards high frequency (e.g. Peureux et al., 2017).

Given that the wave spectrum varies both along the sea surface and with directions, we have to interpolate either in spectral space (from θ to θ') or in physical space (x and y). Simulations indicate that variations in physical space are less severe than those in directions, as illustrated on Figure A1, over a Gulf Stream ring where the Stokes drift is enhanced by wind blowing against the current. We thus estimate $U_{S,R}$ using

$$
U_{S,R}(x,y,\theta) \simeq \sum \cos(\theta - \theta')U_{S,1D}(x',y',\theta')\Delta_{\theta}', \tag{A2}
$$

where the sum is over all directions, and the approximation is due to the fact that the location (x,y) is different from (x',y') where the contribution $U_{S,1D}(x',y',\theta')$ is measured. In practice we use the locations (x',y') that have the right azmuth θ', and that are closest to (x,y), separated by a distance $r(\theta')$. The variations of $U_{S,1D}(\theta')$ over the distance $r(\theta')$, which is typically less than 50 km, is mostly due to the effect of currents on waves (Ardhuin et al., 2017b).

In our simulations we have also varied the beam rotation speed, number of beams and number of azimuths per rotation. Because these parameters give different locations of footprints we have used an approximation of the radial Stokes drift $U_{S,R}$ from the map of Stokes drift vectors instead of the full directional spectrum, this is

$$
U_{S,R}(x,y,\theta) \simeq \frac{2}{\pi}\sum U_{S,R}(x',y',\theta')\cos(\theta - \theta')\Delta_{\theta}', \tag{A3}
$$
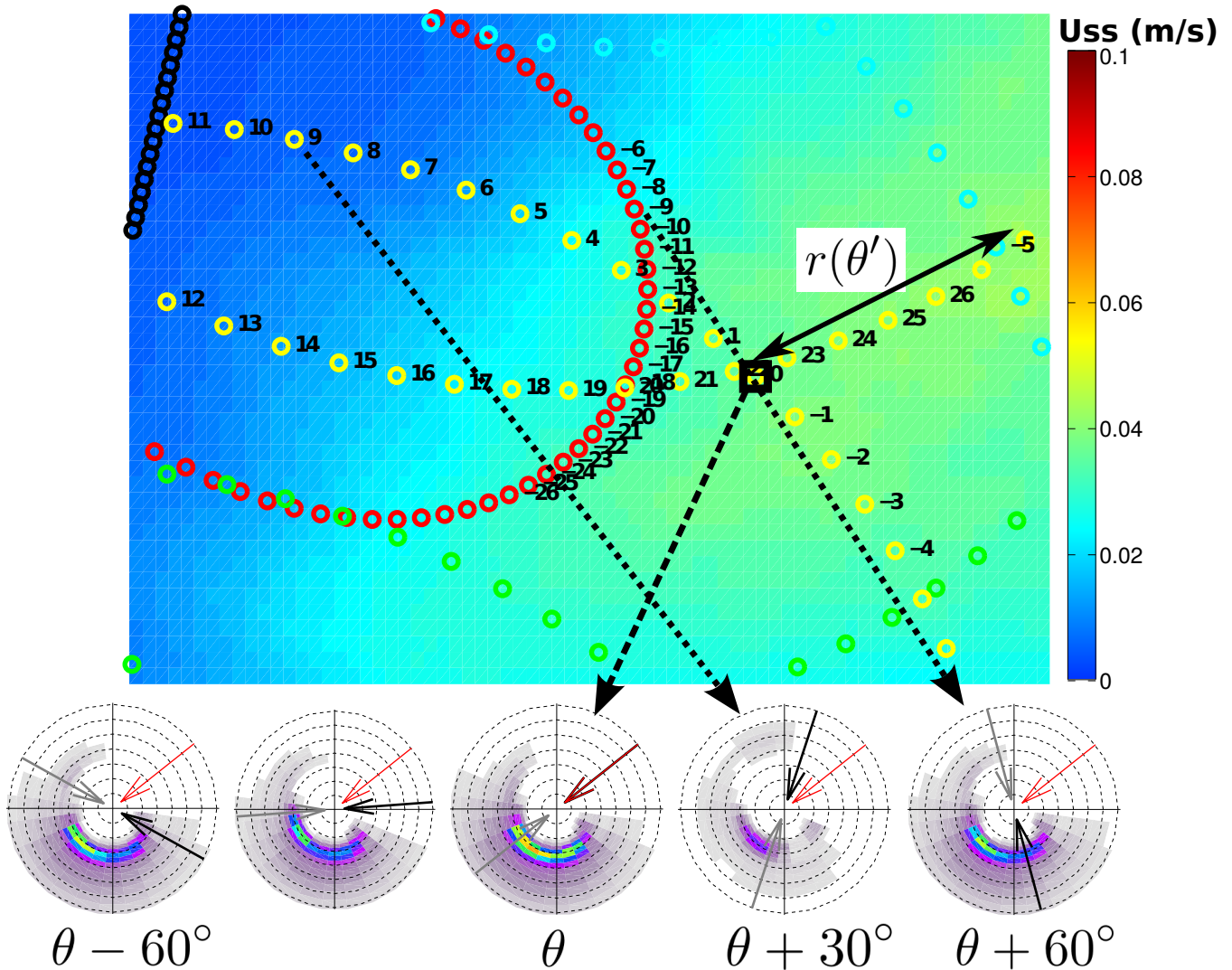
Figure A1. Use of cycles in azimuth θ' for the estimation of the integrated parameters at the location of cycle with direction θ (black square numbered 0). The background color shows the magnitude of U_S. The circles are the location of footprints for azimuths $\theta - \pi/2$, numbered -26, to $\theta + \pi/2$, numbered 26. The distance $r(\theta')$ is a source of error. The bottom wave spectra $E(f, \theta)$ are at the location of different cycles, with wave energy plotted in the direction from which it arrives. In each spectra the red arrow is direction θ, and the black and grey arrows show θ' and $\theta' + \pi$, the dashed circles correspond to frequencies 0.1 to 0.7 Hz. This pattern of footprints correspond to a 6-beam 'SKIM1' configuration (The SKIM Team, 2017), with 108 azimuths. The SKIM2 configuration with 8 beams and 60 azimuths gives an average distance $r(\theta')$ that is 15 to 30% shorter, leading to smaller errors in the estimation of U_{WB}. This is why SKIM2 is used in the present paper.

where the sum is over angles $\theta - \pi/2 < \theta' < \theta + \pi/2$ and the nearest avaible footprints with these azimuths are taken. Eq. (A3) relies on the assumption of small variability of the vector (U_S, V_S) on the scale of the beam rotation. Indeed,$U_{S,R}(\theta)$ is the projection of (U_S, V_S) in direction θ. If (U_S, V_S) is uniform in space then $U_{S,R} = |U_S, V_S| \cos(\theta - \theta_0)$, with θ_0 the direction of the Stokes drift vector. This approximation gives errors in $U_{S,R}(\theta)$ that are typically less than 3%.

5   We have performed realistic high-resolution simulations in a wide range of conditions: Oregon coast, Gulf Stream, equatorial currents, Fram strait, Agulhas current, for which Based on all these simulations and assuming a constant G, we find that the error err_{WB} that is only due to an error in the estimate of $U_{S,R}$, has a negligible bias and a standard deviation that is of the order of,

$$\mathrm{std}(\mathrm{err}_{\mathrm{WB}}) \simeq \varepsilon G \, \mathrm{std}(U_S) \, r_2/20\mathrm{km} \tag{A4}$$

10   where ε is a non-dimensional factor which ranges from 0.10 in the case of the Equator near 23 W, to 0.18 in the Gulf Stream case. $\mathrm{std}(U_S)$ is the standard deviation of the Stokes drift magnitude over the region that contribute to $U_{S,R}$ using eq. (A2).

    The distance

$$r_2 = \sqrt{\sum \left[r(\theta')cos(\theta - \theta')\right]^2 / N} \tag{A5}$$

is the root mean square distance, over the N cycles with directions θ' that contribute to the estimation of $U_{S,R}(\theta)$, between
15 the position of the footprint for azimuth θ and the footprints for θ' weighted by $cos(\theta' - \theta)$. Hence, in the open ocean r_2 is completely specified by the geometry of the footprints, itself given by the rotation speed of the horn plate and the number of beams. In the case presented here r_2 is close to 20 km for the $12°$ beams, and 15 km for the $6°$ beams.

    In order to allow for errors due to the variability of G and random errors in the estimation of the wave spectrum, we have used an error twice as large as given by eq. (A4), namely we use

20 $\mathrm{err}_{\mathrm{WB}} = 2G \times \mathrm{err}(U_{S,R})$ (A6)

    The error err_{WB} has smaller scales than both U_R and $U_{S,R}$, as shown in figure A2. The largest errors are associated with current gradients. This suggests that using some knowledge on wave-current interactions could lead to smaller errors.

Appendix B: Attitude restitution using antenna rotation

The non-geophysical contribution to the Doppler centroïd frequency (f_{NG}) arises from the acquisition geometry (satellite
25 attitude and instrument pointing) and the platform velocity. This frequency is much higher than the geophysical frequency, and it must be estimated carefully. Its theoretical expression is

$$
\begin{aligned}
f_{\mathrm{NG}} \quad = \quad & \frac{2V_{sc}}{\lambda} \sin\gamma \cos\theta \\
& \times \left[1 - \frac{\omega_e}{\omega} (\epsilon \cos\beta \sin\Psi \tan\theta + \cos\Psi) \right] \\
& + \frac{2V_{sc}}{\lambda} e \cos\gamma \frac{\sin(\beta - p)}{\sqrt{1 + e^2 + 2e\cos(\beta - p)}},
\end{aligned}
\tag{B1}
$$
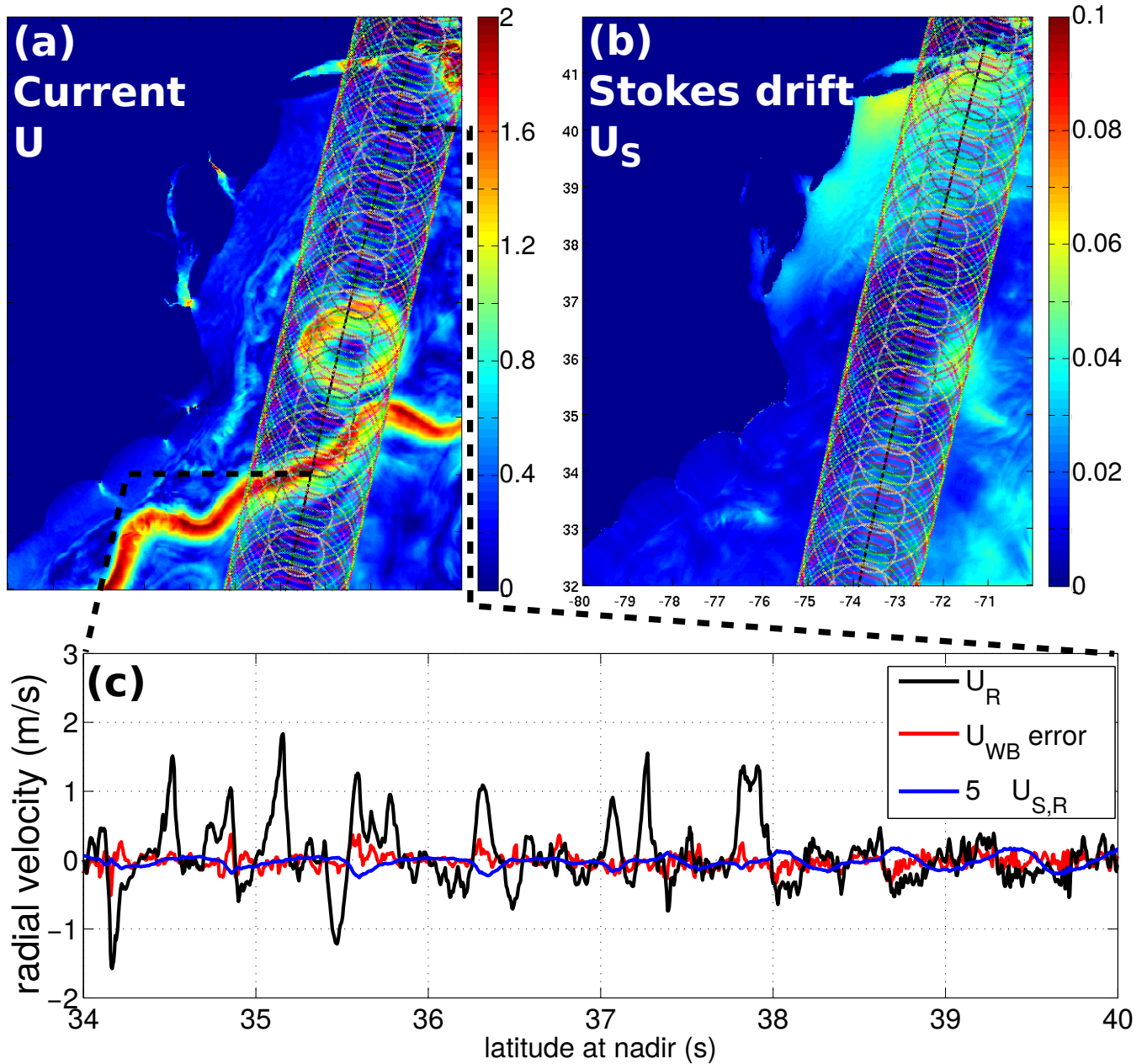
Figure A2. Example of (a) current in the Gulf Stream and associated (b) Stokes drift, and (c) errors for the estimation of UWB for beam 8 (12° incidence, green circles in top panels). In this example the standard deviation of err_{WB} given by eq. (A6) is 10 cm/s, which is of the order of $5U_{S,R}$. Note that the measured geophysical Doppler is $U_{\text{GD}} = U_{\text{WB}} + GU_{S,R}$ with $G \simeq 25$.

where λ is the radar wavelength, V_{sc} is the spacecraft velocity, γ is the elevation angle, θ is the azimuth angle, ϵ is equal to 1 if $\theta \in [0, -\pi]$ and -1 otherwise, ω_e is the angular rotation rate of the Earth, ω is the angular rotation rate of the spacecraft, is Ψ the angular position on the orbit, e is the eccentricity of the orbit, p the argument of the perigee.

All the parameters of f_{NG} are well determined expect for the azimuth and the elevation of the radar beam. The pointing knowledge (around $0.2°$ in elevation and $0.5°$ in azimuth) is not sufficient to get accurate retrieval of f_{NG}. However, compared to Sentinel-1 for which the retrieval of these parameters is complicated, we can use the rotation of the antenna beams in the case of SKIM. The expected variations of the full Doppler centroid $f_{\mathrm{DC}} = f_{\mathrm{NG}} + f_{\mathrm{GD}}$ over one or several full rotations can be used

5 to estimate the Doppler centroid frequency. Here we demonstrate the use of a matching algorithm, based on a Nelder-Mead optimization.

We have assumed that

- the antenna rotation speed is very well known and very stable (it can also be re-estimated after launch on a regular basis),

- the satellite attitude varies slowly (the requirement is below $10^{-4°}$/s,

10 - the estimation of all $12°$ beams are combined over an antenna rotation to increase the azimuth sampling.

Simulations have been performed based on a Monte-Carlo approach with 200 runs. From Eq. B1, frequency signals are generated taking into account noise sources. One source is the coherency loss (SNR impact). Another is the residual wave contribution at the footprint scale, for which we first used a random uniformly distributed noise in the range $[-1, 1]$ m/s.

First simulations have been run with no platform attitude and with only random residual contributions of waves. In this case,

15 the impact of the attitude misknowledge is tested. These angles are injected in the prior solution of the optimization. No impact of the prior knowledge is found, and the maximum error on Doppler velocity is found to be under 0.015 m/s.

Additional simulations have been done to include linear variations of the platform attitude during the rotation and realisting geophysical Doppler contributions f_{GD} from surface currents and wave-induced biases estimated from numerical models MITgcm and WAVEWATCH III. The case of Oregon area is illustrated in Fig B1. The velocity error is very small (< 0.025

20 m/s). The algorithm has been tested on other regions (not illustrated here) with similar results.

Author contributions. All authors have contributed to the writing of the paper. The wave bias error analysis was performed by FA, GM and EC analyzed the Doppler centroid estimation error, and CT and EC analyzed the error due to platform attitude. LG and CU combined these errors to produce simulated data that was used by JX for DFS analysis with TOPAZ. The optimal interpolation scheme was adapted by CU and will be described elsewhere in more details.

25 *Competing interests.* The authors declare that they have no conflict of interest.

Acknowledgements. Support from LabexMer via grant ANR-10-LABX-19-01, and Copernicus Marine Environment Monitoring Service (CMEMS) as part of the Service Evolution program is gratefully acknowledged. Additional support from CNES was given through the VASCO phase 0 study and R&T contracts.
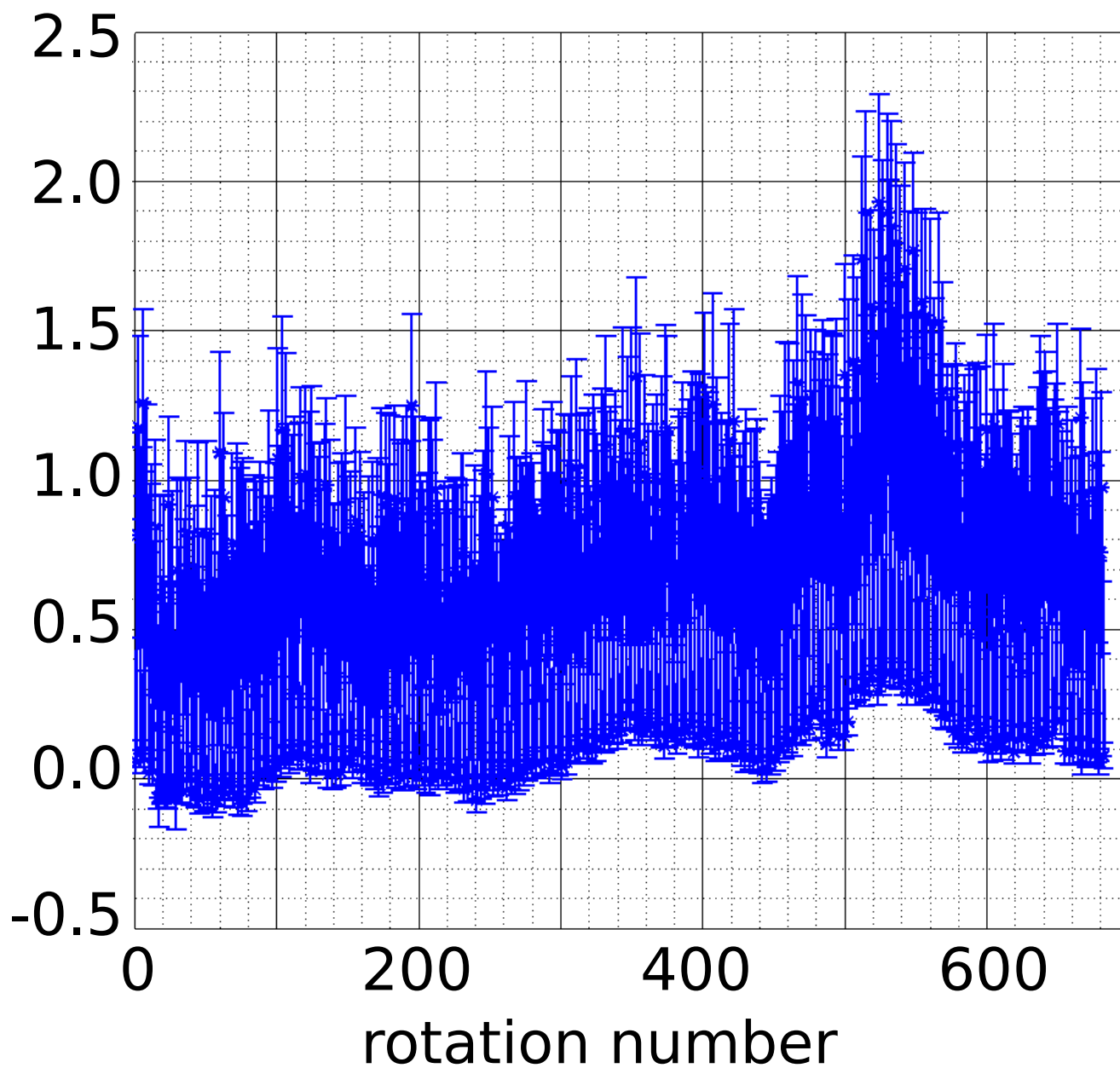
Figure B1. Maxximum velocity residual error (in cm/s) for the Oregon coast simulations. The Doppler centroid has been estimated for a fixed SKIM track over Oregon area. All WW3 run times of month 2014/09 are considered.

References

Aksenov, Y., Popova, E. E., Yool, A., Nurser, A. G., Williams, T. D., Bertino, L., and Bergh, J.: On the future navigability of Arctic sea routes: High-resolution projections of the Arctic Ocean and sea ice, Marine Policy, 75, 300–317, doi:10.1016/j.marpol.2015.12.027, 2017.

Ardhuin, F., Marié, L., Rascle, N., Forget, P., and Roland, A.: Observation and estimation of Lagrangian, Stokes and Eulerian currents induced by wind and waves at the sea surface, J. Phys. Oceanogr., 39, 2820–2838, doi:10.1175/2009JPO4169.1, http://journals.ametsoc.org/doi/pdf/10.1175/2009JPO4169.1, 2009.

Ardhuin, F., Chapron, B., Collard, F., Smith, M., Stopa, J., Thomson, J., Doble, M., Wadhams, P., Blomquist, B., Persson, O., and Collins,
5   III, C. O.: Measuring ocean waves in sea ice using SAR imagery: A quasi-deterministic approach evaluated with Sentinel-1 and in situ data, Remote sensing of Environment, 189, 211–222, doi:10.1016/j.rse.2016.11.024, 2017a.

Ardhuin, F., Rascle, N., Chapron, B., Gula, J., Molemaker, J., Gille, S. T., Menemenlis, D., and Rocha, C.: Small scale currents have large effects on wind wave heights, J. Geophys. Res., 122, doi:10.1002/2016JC012413, in press, 2017b.

Barrick, D. E.: First order theory and analysis of MF/HF/VHF scatter from the sea, IEEE Trans. Antennas Propagat., AP-20, 2–10, 1972.

10   Bonjean, F. and Lagerloef, G. S. E.: Diagnostic Model and Analysis of the Surface Currents in the Tropical Pacific Ocean, J. Phys. Oceanogr., 32, 2938–2954, doi:10.1175/1520-0485(2002)032<2938:DMAAOT>2.0.CO;2, 2002.

Bourassa, M. A., Rodriguez, E., and Chelton, D.: Winds and current mission: Ability to observe mesoscale air/sea coupling, in: Proceedings of IEEE International Geoscience and Remote Sensing Symposium (IGARSS), pp. 7392–7395, IEEE, doi:10.1109/IGARSS.2016.7730928, 2016.

15   Buck, C.: An extension to the wide swath ocean altimeter concept, in: Proceedings of the IEEE International Geoscience and Remote Sensing Symposium (IGARSS), 2013., vol. 8, pp. 543–5439, IEEE, doi:10.1109/IGARSS.2005.1525970, 2005.

Cardinali, C., Pezzulli, S., and Andersson, E.: Influence-matrix diagnostic of a data assimilation system, Q. J. R. Meteorol. Soc., 130, 2767–2786, 2004.

Caudal, G., Hauser, D., Valentin, R., and Gac, C. L.: KuROS: A New Airborne Ku-Band Doppler Radar for Observation of Surfaces, J.
20   Atmos. Ocean Technol., 31, 2023–2245, doi:10.1175/JTECH-D-14-00013.1, 2014.

Chapron, B., Collard, F., and Ardhuin, F.: Direct measurements of ocean surface velocity from space: interpretation and validation, J. Geophys. Res., 110, doi:10.1029/2004JC002809, 2005.

Collard, F., Mouche, A., Chapron, B., Danilo, C., and Johannessen, J.: Routine High Resolution Observation Of Selected Major Surface Currents From Space, in: Proceedings of SEASAR 2008, SP-656, ESA, ESA - ESRIN, Frascati, Italy, http://earth.esa.int/workshops/
25   seasar2008/participants/287/pres_287_Collard.pdf, 2008.

Cravatte, S., Kessler, W. S., Smith, N., Wijffels, S. E., and Contributing Authors: First Report of TPOS, Tech. Rep. 215, GOOS, http://tpos2020.org/first-report/, 2016.

Elfouhaily, T., Chapron, B., Katsaros, K., and Vandemark, D.: A unified directional spectrum for long and short wind-driven waves, J. Geophys. Res., 102, 15 781–15 796, 1997.

30   Elipot, S., Lumpkin, R., Perez, R. C., Lilly, J. M., Early, J. J., and Sykulski, A. M.: A global surface drifter data set at hourly resolution, J. Geophys. Res., 121, 2937–2966, doi:10.1002/2016JC011716, 2016.

Forget, P., Saillard, M., and Broche, P.: Observations of the sea surface by coherent L band radar at low grazing angles in a nearshore environment, J. Geophys. Res., 111, C09 015, doi:10.1029/2005JC002900, 2006.

Forget, P., Saillard, M., Guérin, C.-A., Testud, J., and Bouar, E. L.: On the Use of X-Band Weather Radar for Wind Field Retrieval in Coastal
35   Zone, J. Atmos. Ocean Technol., 82, 899–917, doi:10.1175/JTECH-D-15-0206.1, 2016.

Fu, L.-L. and Ubelmann, C.: On the Transition from Profile Altimeter to Swath Altimeter for Observing Global Ocean Surface Topography, J. Atmos. Ocean Technol., 31, 560–568, 2014.

Gille, S. T. and Hughes, C. W.: Aliasing of high-frequency variability by altimetry: Evaluation from bottom pressure recorders, Geophys. Res. Lett., 28, 1755–1758, doi:10.1029/1999GL011263, 2001.

Goldstein, R. M. and Zebker, H. A.: Interferometric radar measurement of ocean surface current, Nature, 328, 707–709, 1987.

Gula, J., Molemaker, M. J., and Mcwilliams, J. C.: Gulf Stream Dynamics along the Southeastern U.S. Seaboard, J. Phys. Oceanogr., 45, 690–715, 2015.

Hauser, D., Tison, C., Amiot, T., Delaye, L., Corcoral, N., and Castillan, P.: SWIM: The First Spaceborne Wave Scatterometer, IEEE Trans. on Geosci. and Remote Sensing, 55, 3000–3014, 2017.

Horvat, C., Tziperman, E., and Campin, J.-M.: Interaction of sea ice floe size, ocean eddies and sea ice melting, Geophys. Res. Lett., 43, 8083–8090, doi:10.1002/2016GL069742, 2016.

Isern-Fontanet, J., Lapeyre, G., Roullet, G., Danioux, E., Chapron, B., Le Gentil, S., and Sasaki, H.: Retrieval and assimilation of velocities at the ocean surface, Nonlin. Processes Geophys. Discuss., doi:10.5194/npg-2017-14, 2017.

Jackson, F. C., Walton, W. T., and Peng, C. Y.: A comparison of in situ and airborne radar observations of ocean wave directionality, J. Geophys. Res., 90, 1005–1018, 1985.

Jenkins, A. D.: The use of a wave prediction model for driving a near-surface current model, Deut. Hydrogr. Z., 42, 133–149, 1989.

Johannessen, O. M., Johannessen, J. A., Morison, J., Farrelly, B. A., and Svendsen, E. A. S.: OceanographicC onditionsi n the Marginal Ice Zone North of Svalbard in Early Fall 1979 With an Emphasis on Mesoscale Processes, J. Geophys. Res., 88, 2755–2769, 1983.

Kenyon, K. E.: Stokes drift for random gravity waves, J. Geophys. Res., 74, 6991–6994, 1969.

Kim, S. Y., Terrill, E. J., and Cornuelle, B. D.: Mapping surface currents from HF radar radial velocity measurements using optimal interpolation, J. Geophys. Res., 113, C10 023, doi:10.1029/2007JC004244, 2008.

Korosov, A. A. and Rampal, P.: A Combination of Feature Tracking and Pattern Matching with Optimal Parametrization for Sea Ice Drift Retrieval from SAR Data, Remote Sens., 9, 258, doi:10.3390/rs9030258, 2017.

Kuik, A. J., van Vledder, G. P., and Holthuijsen, L. H.: A method for the routine analysis of pitch-and-roll buoy wave data, J. Phys. Oceanogr., 18, 1020–1034, http://journals.ametsoc.org/doi/pdf/10.1175/1520-0485%281987%29017%3C0845%3ATROWDT%3E2.0.CO%3B2, 1988.

Lipa, B. J. and Barrick, D. E.: Least-squares methods for the extraction of surface currents from CODAR crossed-loop data: Application at ARSLOE, IEEE J. Oceanic Eng., 8, 226–253, 1983.

Martin, A. C. H., Gommenginger, C., Marquez, J., Doody, S., Navarro, V., and Buck, C.: Wind-wave-induced velocity in ATI SAR ocean surface currents: First experimental evidence from an airborne campaign, J. Geophys. Res., 121, 1640–1653, doi:10.1002/2015JC011459, 2016.

Mouche, A. A., Chapron, B., and Reul, N.: Predicted Doppler shifts induced by ocean surface wave displacements using asymptotic electromagnetic wave scattering theories, Waves in Random and Complex Media, 18, doi:10.1080/17455030701564644, 2008.

Nouguier, F., Mouche, A., Rascle, N., Chapron, B., and Vandemark, D.: Analysis of Dual-Frequency Ocean Backscatter Measurements at Ku- and Ka-Bands Using Near-Nadir Incidence GPM Radar Data, IEEE Geoscience And Remote Sensing Letters, 31, 2023–2245, doi:10.1109/LGRS.2016.2583198, 2016.

Peureux, C., Benetazzo, A., and Ardhuin, F.: Note on the directional properties of meter-scale gravity waves, Ocean Science Discussions, 2017.

Ponte, A. L., Klein, P., Dunphy, M., and Le Gentil, S.: Low-mode internal tides and balanced dynamics disentanglement in altimetric observations: Synergy with surface density observations, J. Geophys. Res., 122, 2143–2155, doi:10.1002/2016JC012214, 2017.

Rascle, N. and Ardhuin, F.: A global wave parameter database for geophysical applications. Part 2: model validation with improved source term parameterization, Ocean Modelling, 70, 174–188, doi:10.1016/j.ocemod.2012.12.001, 2013.

Rio, M.-H., Mulet, S., and Picot, N.: Beyond GOCE for the ocean circulation estimate: Synergetic use of altimetry, gravimetry, and in situ data provides new insight into geostrophic and Ekman currents, Geophys. Res. Lett., 41, 8918–8925, doi:10.1002/2014GL061773, 2014.

5 Rocha, C. B., Chereskin, T. K., and Gille, S. T.: Mesoscale to Submesoscale Wavenumber Spectra in Drake Passage, J. Phys. Oceanogr., 46, 601–620, doi:10.1175/JPO-D-15-0087.1, 2016.

Romeiser, R., Runge, H., Suchandt, S., Kahle, R., Rossi, C., and Bell, P.: Comparison Of Current Fields From Terrasar-X And Tandem-X Along-Track Interferometry And Doppler Centroid Analysis, in: Proceedings of the IEEE International Geoscience and Remote Sensing Symposium (IGARSS), 2013., IEEE, 2013.

10 Rouault, M. J., Mouche, A., Collard, F., Johannessen, J. A., and Chapron, B.: Mapping the Agulhas Current from space: An assessment of ASAR surface current velocities, J. Geophys. Res., 41, C10 026, doi:10.1029/2009JC006050, 2010.

Sakov, P., Counillon, F., Bertino, L., Lisæter, K. A., Oke, P. R., and Korablev, A.: TOPAZ4: an ocean-sea ice data assimilation system for the North Atlantic and Arctic, Ocean Sci., 8, 633–656, doi:10.5194/os-8-633-2012, http://www.ocean-sci.net/8/633/2012/, 2012.

Stammer, D., Wunsch, C., and Ponte, R. M.: De-aliasing of global high frequency barotropic motions in altimeter observations, Geophys.
15   Res. Lett., 27, 1175–1176, doi:10.1029/1999GL011263, 2000.

Stokes, G. G.: On the theory of oscillatory waves, Trans. Camb. Phil. Soc., 8, 441–455, 1849.

Sudre, J., Maes, C., and Garçon, V.: On the global estimates of geostrophic and Ekman surface currents, Limnology and Oceanography: Fluids and Environments, 3, 1–20, doi:10.1215/21573689-2071927, 2013.

Sutherland, P. and Gascard, J. C.: Airborne remote sensing of ocean wave directional wavenumber spectra in the marginal ice zone, Geophys.
20   Res. Lett., 43, 4659–4664, doi:10.1002/grl.53444, 2016.

The SKIM Team: Sea surface KInematics Multiscale monitoring, full proposal for ESA EE9, Tech. rep., Laboratoire d'Océanographie Physique et Spatiale, Brest, France, doi:10.13140/RG.2.2.18902.86084/1, prepared for European Space Agency, 192 pp., 2017.

Thomson, J., D'Asaro, E. A., Cronin, M. F., Rogers, W. E., Harcourt, R. R., and Shcherbina, A.: Waves and the equilibrium range at Ocean Weather Station P, J. Geophys. Res., 118, 595–5962, doi:10.1002/2013JC008837, 2013.

25 Ubelmann, C., Cornuelle, B., and Fu, L.-L.: Dynamic Mapping of Along-Track Ocean Altimetry: Method and Performance from Observing System Simulation Experiments, J. Atmos. Ocean Technol., 33, 1691–1699, doi:10.1175/JTECH-D-15-0163.1, 2016.

van Sebille, E., Wilcox, C., Lebreton, L., Maximenko, N., Hardesty, B. D., van Franeker, J. A., Eriksen, M., Siegel, D., Galgani, F., and Law, K. L.: A global inventory of small floating plastic debris, Environ. Res. Lett., 10, 124 006, doi:10.1088/1748-9326/10/12/124006, 2015.

Wollstadt, S., López-Dekker, P., De Zan, F., and Younis, M.: Design Principles and Considerations for Spaceborne ATI SAR-Based Obser-
30   vations of Ocean Surface Velocity Vectors, IEEE Trans. on Geosci. and Remote Sensing, 99, 1–20, doi:10.1109/TGRS.2017.2692880, 2016.

Xie, J., Bertino, L., Counillon, F., Lisæter, K. A., and Sakov, P.: Quality assessment of the TOPAZ4 reanalysis in the Arctic over the period 1991–2013, Ocean Science, 13, 123–144, doi:10.5194/os-13-123-2017, http://www.ocean-sci.net/13/123/2017/, 2017.

Yurovsky, Y. Y., Kudryavtsev, V. N., Grodsky, S. A., and Chapron, B.: Normalized Radar Backscattering Cross-section and Doppler Shifts of
35   the Sea Surface in Ka-band, in: Proceedings of the Progress In Electromagnetics Research Symposium (PIERS), May 2017, St Petersburg, Russia, IEEE, 2017.